
White Rose Research Online

eprints@whiterose.ac.uk
https://eprints.whiterose.ac.uk
Universities of Leeds, Sheffield and York

Deposited via The University of Leeds.

White Rose Research Online URL for this paper:
https://eprints.whiterose.ac.uk/id/eprint/194238/

Version: Accepted Version

---

**Article:**
Liu, Y, Zhang, X, Toth, P et al. (2023) The role of volatile organic compounds in the oxidation-driven fragmentation of soot particles. Proceedings of the Combustion Institute, 39 (1). pp. 1079-1088. ISSN: 1540-7489

https://doi.org/10.1016/j.proci.2022.07.198

---

© 2022 The Combustion Institute. Published by Elsevier Inc. This is an author produced version of an article published in Proceedings of the Combustion Institute. Uploaded in accordance with the publisher's self-archiving policy. This manuscript version is made available under the CC-BY-NC-ND 4.0 license http://creativecommons.org/licenses/by-nc-nd/4.0/.

**Reuse**
This article is distributed under the terms of the Creative Commons Attribution-NonCommercial-NoDerivs (CC BY-NC-ND) licence. This licence only allows you to download this work and share it with others as long as you credit the authors, but you can't change the article in any way or use it commercially. More information and the full terms of the licence here: https://creativecommons.org/licenses/

**Takedown**
If you consider content in White Rose Research Online to be in breach of UK law, please notify us by emailing eprints@whiterose.ac.uk including the URL of the record and the reason for the withdrawal request.





# The role of volatile organic compounds in the oxidation-driven fragmentation of soot particles

Ye Liu[a,b,1], Xuyang Zhang[a,1], Pal Toth[c], Wei Zhang[a], Gang Lyu[a], Yunqiang Li[a], Chonglin Song[a,*]

[a] *State Key Laboratory of Engines, Tianjin University, Tianjin 300072, China*
[b] *Institute for Transport Studies, University of Leeds, Leeds LS2 9JT, UK*
[c] *Department of Combustion Technology and Thermal Energy, University of Miskolc, Miskolc, Hungary*

---

**Abstract**

In this work, the role of volatile organic compounds (VOCs) in soot oxidation and fragmentation was investigated in a $CH_4$ lean premixed flame. An aerosol generator was used to homogeneously disperse soot with and without VOCs (termed Soot-W and Soot-WO, respectively) into the flame. Because minimal soot was formed in this flame itself, information on the fragmentation of the Soot-W and Soot-WO during the oxidation process was readily captured to determine the role of VOCs in soot fragmentation. The results of the integrated number concentration of fine mode particles and the degree of particle aggregation show that the presence of VOCs suppresses soot aggregate fragmentation, which is primarily caused by the mitigated consumption of the neck sites between primary particles as a result of the decreased specific surface area. The actual oxygen diffusion route and effective pore width between the crystallite structures were determined using the image analysis technique. The effectiveness factor estimated based on the determined data indicates that the presence of VOCs decreases the possibility of internal burning by oxygen molecules diffusing into primary particles, reducing the extent of primary particle fragmentation, as evidenced by a relatively smaller peak value of ultrafine particles. The analysis of the nanostructure of neck sites vs. the bulk discovers significantly more disordered and thus reactive structure at neck sites, explaining the preferential aggregate fragmentation over primary particle fragmentation. The finding of the role of VOCs in oxidation-driven fragmentation is beneficial to the optimization of existing models for predicting the number concentration of fine and ultrafine particles. Furthermore, a better understanding of this role may aid in the control of the most harmful fine and ultrafine particle emissions.

*Keywords:* Soot oxidation; Aggregate fragmentation; Primary particle fragmentation; Volatile organic compounds; Effectiveness factor

---

*Corresponding author.
*E-mail address*: songchonglin@tju.edu.cn (C.-L. Song)
[1]These authors contributed equally to this work.

## 1. Introduction

Soot fragmentation is a crucial event during the soot oxidation process because it generates a large number of fine and ultrafine particles [1-3]. These fine and ultrafine particles not only have detrimental effects on the environment and human health [4], but also affect the accuracy of existing models to predict the number concentration of oxidized soot particles [2,3,5]. Thus, increasing attention has been paid to oxidation-driven soot fragmentation. The oxidation-driven fragmentation can take place through two mechanisms: (1) the neck sites that keep primary particles together are consumed at a high rate, which causes the fragmentation of soot aggregates [1,2,6,7]; (2) the oxygen penetrates into the primary particle, which results in internal burning and loss of the connectivity between the carbonaceous phases, leading to the fragmentation of primary particles [6-8]. The oxidation-driven soot fragmentation was first experimentally observed by Neoh et al. [8,9] in a two-stage burner, where a drop in particle mass and size was accompanied by a substantial increase in ultrafine particle number concentration. Sediako et al. [10] used environmental transmission electron microscopy to monitor the oxidation of soot aggregate in real-time. They revealed that surface reactions consumed the necks holding primary particles, breaking up aggregates into smaller ones and thus increasing the number concentration of ultrafine particles. Recently, soot fragmentation was investigated by Echavarria et al. [5,6] and Ghiassi et al. [1,2] in a two-stage burner using a scanning mobility particle sizer. A significant increase in the number of soot particles with mobility diameters smaller than 10 nm was found after soot fragmentation. In addition, Zhang et al. [11] and Harris et al. [12] showed that the model prediction of soot particle mobility diameter during oxidation was distinct from the experimental data if the fragmentation event was not taken into consideration.

Volatile organic compounds (VOCs) absorbed on the surface of soot particles originate from unburned hydrocarbons [13]. In general, VOCs account for 5−60% of the total mass of soot particles, depending on the fuel composition and combustion conditions [14]. The presence of VOCs on the surface of soot particles reduces specific surface area and covers porous structure [15]. A decrease in the specific surface area of soot particles means fewer sites available for oxygen adsorption, and thus slows down soot oxidation process [16]. Accompanied by the mitigated soot oxidation, the oxidation rates of neck regions between primary particles are lessened, which in turn weakens the aggregate fragmentation [3,7,10]. In addition, the covered porous structure suppresses oxygen molecules diffusion within the pores of particles, lowering the possibility of internal burning and primary particle fragmentation [1]. In summary, the VOCs probably affect soot fragmentation and significantly alter the emissions of fine and ultrafine particles. Thus, a better understanding of the role of VOCs in soot particle fragmentation can help control the most harmful fine and ultrafine particle emissions. To the best of our knowledge, the role of VOCs in soot aggregate fragmentation and primary particle fragmentation has not been studied before.

In this context, the role of VOCs in the oxidation-driven fragmentation of soot particles, including aggregate fragmentation and primary particle fragmentation, is explored. Soot particles with and without VOCs, respectively, termed Soot-W and Soot-WO, were homogeneously dispersed into a $CH_4$ lean premixed flame via an aerosol generator. Because minimal soot was formed in this flame itself, information on the fragmentation of the Soot-W and Soot-WO during the oxidation process was readily captured to determine the role of VOCs in soot fragmentation.

## 2. Experimental

The schematic diagram of the experimental setup is shown in Fig. S1 of the Supplementary Material. A water-cooled McKenna burner (Holthius and Associates) with a 12.7 mm inner diameter center tube and a 75 mm inner diameter bronze porous plug was employed in this study. The central tube delivered a $CH_4/O_2/N_2$ gas mixture at a cold flow rate of 65 cm/min, producing a $CH_4$ lean premixed flame. An identical mixture was fed through the outer porous plug at a cold flow rate of 4 cm/min to generate a pilot flame that stabilized the center flame. The equivalence ratios of both the center and pilot flames were set at 0.9. The burner was placed on a motorized translation stage with a positional precision of ±0.005 mm, which allowed for the adjustment of the sampling position along the flame's axial direction. Soot particles were sampled from diesel engine exhaust. For a portion of soot particles, isothermal thermal treatment at 450 °C in a nitrogen environment was performed in a thermogravimetric analyzer (Mettler-Toledo TGA/DSC1) for 60 min to remove VOCs [17]. In the pristine diesel soot samples, VOCs account for around 11% of the total mass of soot particles. After thorough grinding in an agate mortar, an aerosol generator (Palas RGB-1000-GD) was used to feed Soot-W or Soot-WO into the flame, because the aerosol generator steadily generated solid aerosols at a very low feed rate [18]. Detail on the aerosol generator has been given in [18]. A rotating brush was utilized in the aerosol generator to disperse the soot sample into the $CH_4/O_2/N_2$ stream. To achieve soot dispersion uniformity and consistency during the test, a fast rotation speed of the brush (1200 rpm) and a small feed rate (1 mm/h) were employed. To validate the feasibility of this method, the particle size distributions (PSDs) of the Soot-W and Soot-WO at the burner center were measured before the flame was ignited at HAB = 0 mm. As seen in Fig. S2 of the Supplementary Material, the PSDs for both Soot-W and Soot-WO are almost identical, indicating that the Soot-W and Soot-WO were homogeneously and

consistently dispersed into the $CH_4/O_2/N_2$ stream. In addition, the particles formed by the $CH_4$ combustion in the lean flame were examined, and it was found that the integrated number concentrations in the flame with soot addition were 3-5 orders of magnitude higher than those without soot addition. Hence, the number of particles generated in the flame can be considered negligible.

The visible flame height was 22 mm, as shown in Fig. S3 of the Supplementary Material. The flame temperatures were measured axially using an R-type thermocouple (Pt/Pt13 Rh) with a 30 μm wire and a bead diameter of approximately 150 μm. The acquired temperatures were corrected for radiative heat loss based on the method proposed in [19], and the flame temperature profiles after the dispersion of the Soot-W and Soot-WO are shown in Fig. S4 of the Supplementary Material. The difference in flame temperature for the Soot-W and Soot-WO at the same axial position was within the experimental error (± 50 K). Thus, the effect of temperature can be regarded as negligible. A thermophoretic sampling system was used to obtain the soot particles for the HRTEM analysis. The thermophoretic sampling system included an advanced linear electric cylinder (FESTO, Germany) capable of rapid and precise reciprocating motion with an acceleration and speed of 120 m/s$^2$ and 3 m/s, respectively, and the relative residence time of sampling soot particles was 30 ms. A self-closing tweezer (N5, Switzerland) was mounted on the piston rod to conveniently fix and detach the C/Cu grid that was used to collect soot particles.

The PSDs in the range of 5.6 to 560 nm and the particle number concentrations were measured using an SMPS (TSI 3090). The SMPS sampling system is similar to one developed by Zhao et al. [20]. The dilution ratio was set between $10^2$ and $10^3$ to quench the chemical reactions and limit soot particle coagulation and losses in the sampling tube [5,20]. Corrections for diffusion coagulation and tube losses were made using the approach given by Minutolo et al. [21]. HRTEM (JEOL EM-2010F) with a point resolution of 0.248 nm operating at 200 kV was used to acquire soot morphology and HRTEM images at magnifications of 40,000× and 400,000×, respectively. The HRTEM images were digitized, and lattice fringe analysis was carried out using an automated fringe image processing system (FIPS) to quantify nanostructure characteristics such as fringe length ($L_a$) and tortuosity ($T_f$). Details on the FIPS were reported in our previous study [22]. In addition, the image analysis procedure described by Toth et al. [23,24] was also used to obtain the crystallite tortuosity ($\tau$) and effective pore width ($r_p$) to assess the possibility of internal burning. An example result is shown in Fig. S5 of the Supplementary Material. Soot crystallites are visible in the yellow color, and the white lines represent medial axes of hypothetical paths of oxygen. Tortuosity, the ratio of the actual distance that the $O_2$ must travel to reach the amorphous core to the shortest distance from the particle perimeter to the core, was computed as a Monte-Carlo ensemble of random walk simulations [1,25]. The effective pore width was estimated by assuming that the penetrating oxygen continues its path through the slit-shaped spaces between two crystallites until it reaches the particle's core [1,23]. For each sample, approximately 15 HRTEM images were randomly selected to obtain the average $\tau$ and $r_p$. The specific surface area of the pristine Soot-W and Soot-WO was determined by the Brunauer-Emmett-Teller (BET) method on the micromeritics analyzer (Tristar II 3020) with nitrogen as the adsorption gas at 77K. Due to the limited amount of sample collected in the flame, no analysis of the surface area of soot samples from various HABs was performed. $H_2$, $O_2$, CO, and $CO_2$ in flame were measured using an online gas chromatograph (GC, Agilent 7890A). More details on the online GC measurement method have been reported in the literature [26].

## 3. Results and discussion

### *3.1 Soot aggregate fragmentation*

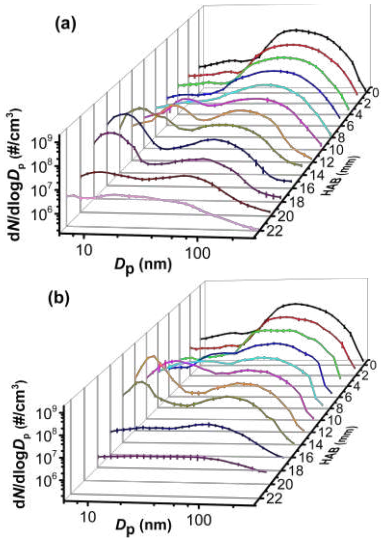



Fig. 1. Particle size distributions (PSDs) as functions of the height above the burner (HAB) for Soot-W (a) and Soot-WO (b). The error bars indicate the standard error.

Figure 1 shows the PSDs of the Soot-W and Soot-WO at various HABs. For both soots, the PSDs are unimodal at low HABs, and gradually shift from the unimodal to bimodal distribution as the HAB increases. The transformation of PSDs from the unimodal to bimodal distribution suggests that soot fragmentation occurs, and a large number of soot particles are generated.

The oxidation-driven fragmentation of soot particles can occur via two mechanisms: aggregate fragmentation and primary particle fragmentation [1,2,6]. Zhang et al. [27] examined the structural evolution of soot particles in a single-cylinder diesel

engine, and reported that a large number of soot particles with the mobility diameter ($D_p$)<30 nm were formed after aggregate fragmentation. In a $C_2H_4$ flame, Sirignano et al. [28] found that the aggregate fragmentation increased the number concentration of the particles with 10<$D_p$<30 nm. According to the findings of Zhang et al. and Sirignano et al., the number concentration of the particles with 10< $D_p$<30 nm (termed fine mode particles) was used to probe the aggregate fragmentation. Figure 2 shows the integrated number concentration of fine mode particles and the overall soot burnout percentages for the Soot-W and the Soot-WO at various HABs. For both soots, the integrated number concentrations remain relatively constant at the low HABs. This behavior suggests that a certain extent of aggregate fragmentation has already taken place in the low regions of the flame, which compensates for the reduction of fine mode particles caused by soot oxidation. At the intermediate HABs, despite a significant increase in the overall soot burnout percentages, both soots exhibit remarkable increases in the integrated number concentrations of fine mode particles, indicating the occurrence of a high extent of aggregate fragmentation. For the Soot-W, the integrated number concentration peaks at approximately HAB=14 mm with a value of $3.38\times10^8$ #/cm$^3$; for the Soot-WO, the number concentration peak locates at approximately HAB=10 mm with a value of $4.17\times10^8$ #/cm$^3$. The above results show that the Soot-W has the delayed appearance of the number concentration peak and the relatively small peak value, inferring that the presence of the VOCs on the particles suppresses the aggregate fragmentation. In the upper region of the flame, the soot oxidation and the gradual reduction of the extent of aggregate fragmentation result in the decreased number concentrations for both soots.

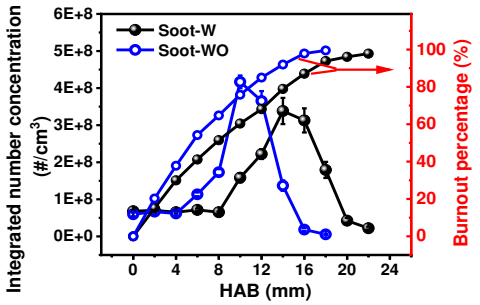



Fig. 2. Integrated number concentrations of the particles with 10<$D_p$<30 nm and the overall soot burnout percentages at various HABs. The error bars indicate the standard error.

Aggregate fragmentation is primarily caused by the breakup of neck regions where primary particles make contact with one another [6,8,10], and thus inevitably reduces the number of primary soot particles per soot aggregate, termed as the degree of particle aggregation ($N_p$) [11,29]. Therefore, the $N_p$ can be used as an indicator of the extent of aggregate fragmentation. That is, a significant decrease in the $N_p$ means a high extent of aggregate fragmentation. In this study, the $N_p$ was explored to support the results presented above. The calculation of $N_p$ was based on the TEM images, and typical TEM images of the samples are shown in Fig. 3. For each HAB, more than 50 soot aggregates were randomly selected for the $N_p$ calculation to ensure statistical significance, and the average values ($\overline{N_p}$) were used to outline the aggregate fragmentation. Fig. 4 shows the $\overline{N_p}$ for the Soot-W and the Soot-WO at different HABs. For the Soot-W, the $\overline{N_p}$ sharply reduces as the HAB increases from 8 to 14 mm, indicating the occurrence of a high extent of aggregate fragmentation. These $\overline{N_p}$ results are consistent with what are in Fig. 2, where in the same HAB range, a significant increase in the number concentrations of the fine mode particles highlights a high extent of aggregate fragmentation for the Soot-W. Likewise, in Figs. 2 and 4, a sharp decrease in the $\overline{N_p}$ and a substantial increase in the number concentrations of fine mode particles are observed in the HAB range of 4–10 mm for the Soot-WO. In addition, the effects of VOCs on the aggregate fragmentation can be detected from the $\overline{N_p}$ results in Fig 4. As seen, the sharp decrease in $\overline{N_p}$ for the Soot-W starts at HAB=8 mm, while the Soot-WO initiates the significant decrease in $\overline{N_p}$ at HAB=4 mm. Such a difference also confirms that the presence of VOCs depresses the aggregate fragmentation.

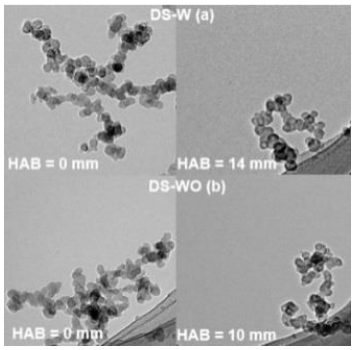



Fig. 3. Typical morphology images of the Soot-W (a) and Soot-WO (b).

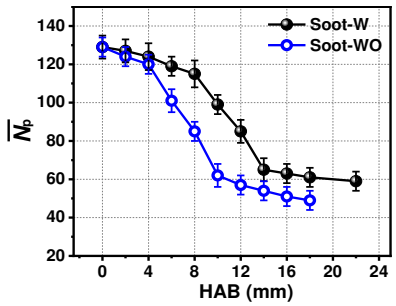



Fig. 4. Average values of particle aggregation degree ($\overline{N_p}$) as a function of height above the burner (HAB). The error bars indicate the standard error.

The results in Figs. 2 and 4 demonstrate the effects of VOCs on the aggregate fragmentation. Because the oxidation environments in the flame (see Figs. S4 and S6 of the Supplementary Material) are quite similar for the Soot-W and Soot-WO, it is speculated that the effects of VOCs on the aggregate fragmentation are primarily ascribed to the different properties between the Soot-W and Soot-WO. To clarify this issue, the nanostructure and specific surface area of the pristine Soot-W and Soot-WO were examined using HRTEM and BET. The fringe length, tortuosity and specific surface area of both soots are listed in Table 1. Considering the uncertainties, no structural differences between the Soot-W and Soot-WO can be identified from this table. However, the Soot-WO has a surface area of 99 $m^2/g$, about 90% larger than that of the Soot-WO. The larger specific surface area means more sites available for oxygen adsorption, and as a consequence, promotes the soot oxidation process. Accompanied by the improved soot oxidation, of course, is the acceleration of the breakup of the neck region between primary particles, which in turn enhances the aggregate fragmentation [3,7,10].

Table 1
Mean fringe length ($L_a$) and tortuosity ($T_f$), and surface area of the pristine Soot-W and Soot-WO.

| Description (units) | Soot-W | Soot-WO |
|---|---|---|
| Mean fringe length (nm) | 1.056 ± 0.047 | 1.059 ± 0.039 |
| Mean fringe tortuosity | 1.362 ± 0.041 | 1.364 ± 0.043 |
| BET surface area ($m^2/g$) | 52 ± 3 | 99 ± 5 |

### *3.2 Primary particle fragmentation*

Because the primary particle fragmentation of substantially enhances the concentration of ultrafine particles ($D_p$<10 nm) [1,3,30], the ultrafine particle concentration was used to evaluate the extent of primary particle fragmentation. Figure 5 shows the integrated number concentrations of the ultrafine particles as functions of HAB. Similar to the concentrations of fine mode particles in Fig. 2, for both the Soot-WO and Soot-W, the integrated number concentrations of ultrafine particles are also relatively constant at low region of flame, and then exhibit significant increases with further increasing the HAB. These results imply that upon soot oxidation, the primary particle fragmentation has occurred, and the high extent of primary particle fragmentation is present at the intermediate HABs. In addition, the peaks of the number concentrations appear at around HAB=12 mm with a value of $1.04\times10^9$ #/$cm^3$ for the Soot-WO and at around HAB=14 mm with a value of $6.72\times10^8$ #/$cm^3$ for the Soot-W. The fact that the Soot-W has a delayed appearance of the number concentration peak and a relatively small peak value confirms that the presence of VOCs on particles depresses the primary particle fragmentation as well. At the upper HABs, the soot oxidation and the gradual reduction of the extent of primary particle fragmentation are responsible for the decreased number concentrations of the ultrafine particles.

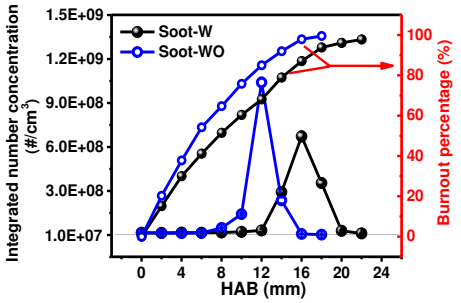



Fig. 5. Integrated number concentrations of ultrafine particles ($D_p$<10 nm) and overall soot burnout percentages at various heights above the burner (HABs). The error bars indicate the standard error.

Different from the aggregate fragmentation, the primary particle fragmentation is mainly caused by oxygen molecules diffusing into the interiors of primary particles to result in internal burning, after which the primary particles break up into small pieces [3,6,7]. Thus, the premise for the occurrence of primary particle fragmentation is internal burning. Because the presence of VOCs decreases the specific surface area of soot particles, as indicated in Table 1, the pristine Soot-W has less porous structure [31,32]. The less porous structure makes it difficult for oxygen molecules to penetrate into the interiors of primary particles, and as a consequence, reduces the possibility of primary particle fragmentation. On the other hand, the differences in the initial oxidation reactivity due to the different specific surface areas cause both soots to undergo various oxidation histories [16], which in turn alters soot internal structure [33]. Because soot structure is closely associated with the oxygen diffusion pathways into the interiors of soot particles [1], the structural alteration inevitably affects the internal burning. In this study, the effectiveness factor ($\eta$) was introduced to examine the possibility of the internal burning. When the $\eta$ is close to 1, it indicates that the $O_2$ can penetrate thoroughly into the interiors of soot nanostructure, and result in the internal burning; when the $\eta$ is close to 0, it means that there is only limited or no $O_2$ penetration into the soot nanostructure, and no internal oxidation occurs. Based on the assumption of first-order reaction, the $\eta$ for spherical particles in terms of the Thiele Modulus ($M_T$) can be calculated determined according to Neoh [34]:

$$\eta = \frac{3}{M_T}\left(\frac{1}{tanh\, M_T} - \frac{1}{M_T}\right) \quad (1)$$

where the square of $M_T$ is the ratio of the time required for oxygen diffusion ($T_D$) to the time needed for oxygen reaction ($T_R$), $M_T^2 = T_D/T_R$. $T_D$ is defined as $T_D = R^2/D_e$ [1], where $R$ is the radius of soot particle, and $D_e$ is the effective intra-soot diffusion coefficient, expressed as [1,35,36]:

$$D_e = \frac{4}{3}\frac{\rho S_{BET}}{\tau}\left(\frac{R_g T}{2\pi M}\right)^{\frac{1}{2}} r_p^2 \quad (2)$$

where $\rho$ is soot density; $S_{BET}$ is the surface area ($m^2/g$); $R_g$ is the universal gas constant; $T$ is the temperature ($K$); $M$ is oxygen molecular weight, and $r_p$ and $\tau$ are the effective pore width and crystallite tortuosity, respectively.

The time scale for oxygen reaction ($T_R$) on the soot surface or inside soot particles is a function of the rate constant ($k$) of the Nagle/Strickland-Constable reaction (NSC), $T_R = 1/k$ [1]. Some investigations and our previous study, however, have discovered that the experimental soot oxidation rates were higher than those calculated using the NSC equation [37,38]. Thus, a factor of four higher soot oxidation rate than the NSC rate was used to evaluate $T_R$, as follows [1,38]:

$$T_R = \frac{1}{4k} = \frac{W\rho S_{BET}}{48 C_{O_2}} \quad (3)$$

where $W$ is the soot oxidation rate of NSC ($g/cm^2 \cdot s$); $C_{O2}$ is the oxygen concentration ($mol/cm^2$), obtained by the GC measurement.

Table 2
Effectiveness factor ($\eta$) and key parameters for calculating effectiveness factor.

| HAB | Soot-W | | | | | Soot-WO | | | | |
|---|---|---|---|---|---|---|---|---|---|---|
| (mm) | $O_2$ (mol %) | $d_p$ (nm) | $\tau$ | $r_p$ (nm) | $\eta$ | $O_2$ (mol %) | $d_p$ (nm) | $\tau$ | $r_p$ (nm) | $\eta$ |
| 4 | 2.53 | 20.76 ± 0.24 | 3.57 ± 0.02 | 1.07 ± 0.03 | 0.334 | 2.54 | 20.41 ± 0.17 | 3.52 ± 0.03 | 1.21 ± 0.04 | 0.381 |
| 8 | 2.27 | 19.59 ± 0.23 | 2.87 ± 0.03 | 1.29 ± 0.04 | 0.470 | 2.25 | 19.07 ± 0.21 | 2.71 ± 0.05 | 1.40 ± 0.05 | 0.520 |
| 12 | 2.15 | 18.99 ± 0.17 | 2.52 ± 0.05 | 1.36 ± 0.04 | 0.546 | 2.14 | 18.76 ± 0.20 | 2.17 ± 0.05 | 1.53 ± 0.05 | 0.628 |
| 16 | 2.09 | 18.86 ± 0.24 | 2.37 ± 0.04 | 1.48 ± 0.03 | 0.615 | 2.07 | 18.39 ± 0.18 | 2.35 ± 0.03 | 1.36 ± 0.03 | 0.596 |
| 20 | 2.06 | 18.39 ± 0.21 | 2.73 ± 0.05 | 1.37 ± 0.04 | 0.604 | | | | | |

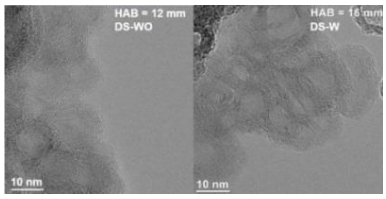


Fig. 6. Typical HRTEM images of the Soot-WO at HAB = 12 mm and Soot-W at HAB = 16 mm.

Based on the above equations, the $\eta$ of the Soot-W and Soot-WO at various HABs were calculated. The calculated results and key parameters for calculating the $\eta$ are summarized in Table 2. As expected, the $\eta$ values peak at HAB = 12 mm for the Soot-WO and at HAB = 16 mm for the Soot-W, where the high extent of the primary particle fragmentation occurs, as evidenced by the highest integrated number concentration of ultrafine mode particles in Fig. 5. Furthermore, the HRTEM analysis provides additional evidence for the occurrence of internal burning. At HAB = 12 mm for the Soot-WO or at HAB = 16 mm for the Soot-W, a large quantity of soot particles with hollow structures is readily observed under the visual field of HRTEM, as shown in Fig. 6. Previous studies [7,39-41] confirmed that such hollow capsule structure for soot particles was a result of internal burning. In addition, the delayed appearance of the peak $\eta$ value for the Soot-W also infers that the presence of VOCs on the soot particles has an unfavorable effect on the primary particle fragmentation. From Table 2, it is noted that at the same HAB, the crystallite tortuosity ($\tau$), pore width ($r_p$), and primary particle size ($d_p$) are different between the Soot-W and Soot-WO, reflecting the differences in soot structure. These results confirm the above conjecture that the presence of VOCs reduces the specific surface area of soot particles and then affects the soot structure during the oxidation process. As a consequence, both soots have different $\eta$ values at the same HAB.

### *3.3. Comparison between the fragmentation of primary particle and aggregate*

In Figs. 2 and 5, it is interesting to note that for both soot samples, the aggregate fragmentation starts at a lower soot burnout percentage than the primary particle fragmentation. Considering that the aggregate fragmentation is caused by the breakup of necks connecting primary particles [6,7], the nanostructure of the neck sites versus the bulk was evaluated to ascertain the rationale for the preferential fragmentation of aggregates. In the present study, structural analysis of the pristine Soot-WO, as a representative, was performed using the HRTEM. More than 20 particle neck and bulk regions in the HRTEM images were chosen randomly to extract the nanostructural parameters using FIPS. The average values of the fringe length and tortuosity are shown in Fig. 7. The soot neck regions have shorter average fringe length and greater fringe tortuosity than the bulk, indicating that the neck regions have a less-ordered nanostructure compared to the bulk. Thus, the neck regions with a less-ordered nanostructure are expected to have higher oxidation rates than the bulk [1,16,17], facilitating the occurrence of aggregate fragmentation. In the soot bulk, the outermost shells have more ordered structures than the intermediate layers and inner core [42]. Thus, the outermost shells of primary particles are more resistant to oxidation than the neck regions. Slow consumption of outermost

shells diminishes oxygen molecules diffusion into primary particles [43,44], and thus prolongs the time required for the penetration of oxygen into the interiors of primary particles and delays the occurrence of internal burning and primary particle fragmentation. Therefore, the aggregate fragmentation occurs in advance to the primary particle fragmentation.

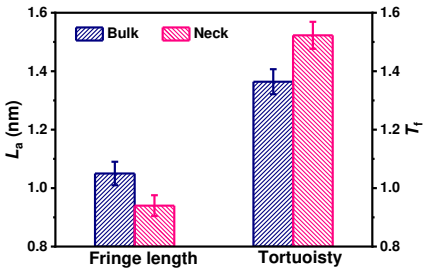



Fig. 7. Fringe length ($L_a$) and tortuosity ($T_f$) for neck and bulk regions of pristine Soot-WO. The error bars indicate the standard error.

A similar result was reported by Echavarria et al. [6], who investigated soot fragmentation in a two-stage burner. They revealed that aggregate fragmentation occurred at a low soot burnout percentage through the breakup of the necks linking primary particles, whereas primary particles fragmented at a high soot burnout percentage through the loss of the connectivity between the carbonaceous phases due to internal burning. In a follow-up study, Toth et al. [7] examined the soot oxidation process using an in-situ spherical aberration-corrected environmental transmission electron microscopy. Their experimental results supported Echavarria's assertion, and they ascribed the preferential occurrence of aggregate fragmentation to exposing more edge sites at the neck versus the bulk, resulting in intensified carbon consumption locally. Ghiassi et al. [1] evaluated the degree of orderliness regarding both nematic (flat) and polar (curvy) symmetry of soot neck and bulk regions. They concluded that the neck sites had a more disordered nanostructure relative to the bulk, thus facilitating the neck consumption.

## 4. Conclusions

In this study, soot particles with and without volatile organic compounds (VOCs), respectively, were homogeneously dispersed into a $CH_4$ lean premixed flame to explore the role of VOCs in aggregate and primary particle fragmentation during oxidation. The oxidation process was thoroughly studied using SMPS and GC, and BET and HRTEM of the pristine and oxidized soot. The results consistently show that the presence of VOCs suppresses the occurrence of aggregate fragmentation and primary particle fragmentation. The aggregate fragmentation occurs in advance to the primary particle fragmentation, regardless of the presence of VOCs or not. The nanostructural analysis about neck sites vs. the bulk finds significantly more disordered and thus reactive structure at neck sites, explaining the preferential aggregate fragmentation over primary particle fragmentation. The results obtained in this study clearly demonstrate that the VOCs can significantly affect soot fragmentation, even if the mass fraction of VOCs is as low as 11%. Thus, existing models should take the VOCs on soot surface into consideration. Furthermore, a better understanding of the role of VOCs in soot particle fragmentation can help control the most harmful fine and ultrafine particle emissions.

## Acknowledgements

This study was supported by the National Natural Science Foundation of China (91741127 and 51921004) and the Program of Tianjin Science and Technology Plan (18PTZWHZ00170).

## Supplementary material

Supplementary material has been submitted along with this manuscript.

## References

[1] H. Ghiassi, P. Toth, I.C. Jaramillo, J.S. Lighty, Soot oxidation-induced fragmentation: Part 1: The relationship between soot nanostructure and oxidation-induced fragmentation, Combust. Flame 163 (2016) 179-187.

[2] H. Ghiassi, I.C. Jaramillo, P. Toth, J.S. Lighty, Soot oxidation-induced fragmentation: Part 2: Experimental investigation of the mechanism of fragmentation, Combust. Flame 163 (2016) 170-178.

[3] M. Sirignano, H. Ghiassi, A. D'Anna, J.S. Lighty, Temperature and oxygen effects on oxidation-induced fragmentation of soot particles, Combust. Flame 171 (2016) 15-26.

[4] A. Lammers, N. Janssen, A. Boere, M. Berger, C. Longo, S. Vijverberg, A. Neerincx, A. Maitland-van der Zee, F. Cassee, Effects of short-term exposures to ultrafine particles near an airport in healthy subjects, Environ. Int. 141 (2020) 105779.

[5] C.A. Echavarria, I.C. Jaramillo, A.F. Sarofim, J.S. Lighty, Studies of soot oxidation and fragmentation in a two-stage burner under fuel-lean and fuel-rich conditions, Proc. Combust. Inst. 33 (2011) 659-666.

[6] C.A. Echavarria, I.C. Jaramillo, A.F. Sarofim, J.S. Lighty, Burnout of soot particles in a two-stage burner with a JP-8 surrogate fuel, Combust. Flame 159 (2012) 2441-2448.

[7] P. Toth, D. Jacobsson, M. Ek, H. Wiinikka, Real-time, in situ, atomic scale observation of soot oxidation, Carbon 145 (2019) 149-160.

[8] K.G. Neoh, J.B. Howard, A.F. Sarofim, Effect of oxidation on the physical structure of soot, Symp. (Int.) Combust. (1985) 951-957.

[9] K. Neoh, J. Howard, A. Sarofim, Soot oxidation in flames, Particulate Carbon, Springer 1981, pp. 261-282.
[10] A.D. Sediako, C. Soong, J.Y. Howe, M.R. Kholghy, M.J. Thomson, Real-time observation of soot aggregate oxidation in an Environmental Transmission Electron Microscope, Proc. Combust. Inst. 36 (2017) 841-851.
[11] Q. Zhang, M.J. Thomson, H. Guo, F. Liu, G.J. Smallwood, Modeling of oxidation-driven soot aggregate fragmentation in a laminar coflow diffusion flame, Combust. Sci. Technol. 182 (2010) 491-504.
[12] S.J. Harris, M.M. Maricq, The role of fragmentation in defining the signature size distribution of diesel soot, J. Aerosol Sci. 33 (2002) 935-942.
[13] K. Al-Qurashi, Y. Zhang, A.L. Boehman, Impact of Intake CO2 Addition and Exhaust Gas Recirculation on NO x Emissions and Soot Reactivity in a Common Rail Diesel Engine, Energy Fuels 26 (2012) 6098-6105.
[14] B.R. Stanmore, J.F. Brilhac, P. Gilot, The oxidation of soot: a review of experiments, mechanisms and models, Carbon 39 (2001) 2247-2268.
[15] T. Ishiguro, N. Suzuki, Y. Fujitani, H. Morimoto, Microstructural changes of diesel soot during oxidation, Combust. Flame 85 (1991) 1-6.
[16] I.C. Jaramillo, C.K. Gaddam, R.L. Vander Wal, J.S. Lighty, Effect of nanostructure, oxidative pressure and extent of oxidation on model carbon reactivity, Combust. Flame 162 (2015) 1848-1856.
[17] K. Yehliu, R.L. Vander Wal, O. Armas, A.L. Boehman, Impact of fuel formulation on the nanostructure and reactivity of diesel soot, Combust. Flame 159 (2012) 3597-3606.
[18] T. Myojo, T. Oyabu, K. Nishi, C. Kadoya, I. Tanaka, M. Ono-Ogasawara, H. Sakae, T. Shirai, Aerosol generation and measurement of multi-wall carbon nanotubes, J. Nanopart. Res. 11 (2009) 91-99.
[19] C.S. McEnally, Ü.Ö. Köylü, L.D. Pfefferle, D.E. Rosner, Soot volume fraction and temperature measurements in laminar nonpremixed flames using thermocouples, Combust. Flame 109 (1997) 701-720.
[20] B. Zhao, Z. Yang, J. Wang, M.V. Johnston, H. Wang, Analysis of Soot Nanoparticles in a Laminar Premixed Ethylene Flame by Scanning Mobility Particle Sizer, Aerosol Sci. Technol. 37 (2003) 611-620.
[21] P. Minutolo, A. D'Anna, A. D'Alessio, On detection of nanoparticles below the sooting threshold, Combust. Flame 152 (2008) 287-292.
[22] Y. Liu, C. Song, G. Lv, W. Zhang, H. Chen, Evaluation of the oxidative reactivity and electrical properties of soot particles, Carbon 178 (2021) 37-47.
[23] P. Toth, A.B. Palotas, T.A. Ring, E.G. Eddings, R. Vander Wal, J.S. Lighty, The effect of oxidation pressure on the equilibrium nanostructure of soot particles, Combust. Flame 162 (2015) 2422-2430.
[24] P. Toth, Á.B. Palotás, J. Lighty, C.A. Echavarria, Quantitative differentiation of poorly ordered soot nanostructures: A semi-empirical approach, Fuel 99 (2012) 1-8.
[25] P. Pré, G. Huchet, D. Jeulin, J.-N. Rouzaud, M. Sennour, A. Thorel, A new approach to characterize the nanostructure of activated carbons from mathematical morphology applied to high resolution transmission electron microscopy images, Carbon 52 (2013) 239-258.
[26] M.J. Castaldi, A.M. Vincitore, S.M. Senkan, Micro-Structures of Premixed Hydrocarbon Flames: Methane, Combust. Sci. Technol. 107 (1995) 1-19.
[27] R. Zhang, S. Kook, Structural evolution of soot particles during diesel combustion in a single-cylinder light-duty engine, Combust. Flame 162 (2015) 2720-2728.
[28] M. Sirignano, J. Kent, A. D'Anna, Further experimental and modelling evidences of soot fragmentation in flames, Proc. Combust. Inst. 35 (2015) 1779-1786.
[29] R. Puri, T.F. Richardson, R.J. Santoro, R.A. Dobbins, Aerosol dynamic processes of soot aggregates in a laminar ethene diffusion flame, Combust. Flame 92 (1993) 320-333.
[30] H. Ghiassi, Soot oxidation and the mechanisms of oxidation-induced fragmentation in a two-stage burner fro ethylene and surrogate fuels, PhD thesis, The University of Utah, (2015).
[31] R.T. Yang, C. Wong, Kinetics and mechanism of oxidation of basal plane on graphite, J. Chem. Phys. 75 (1981) 4471-4476.
[32] R.T. Yang, C. Wong, Mechanism of single-layer graphite oxidation: evaluation by electron microscopy, Science 214 (1981) 437-438.
[33] R.L. Vander Wal, A. Yezerets, N.W. Currier, D.H. Kim, C.M. Wang, HRTEM Study of diesel soot collected from diesel particulate filters, Carbon 45 (2007) 70-77.
[34] K. Neoh, Soot burnout in flames, PhD thesis, Massachusetts Institute of Technology, (1980).
[35] W. Kast, C.-R. Hohenthanner, Mass transfer within the gas-phase of porous media, Int. J. Heat Mass Transfer 43 (2000) 807-823.
[36] J.F. Brilhac, F. Bensouda, P. Gilot, A. Brillard, B. Stanmore, Experimental and theoretical study of oxygen diffusion within packed beds of carbon black, Carbon 38 (2000) 1011-1019.
[37] R.L. Vander Wal, A.J. Tomasek, Soot oxidation: dependence upon initial nanostructure, Combust. Flame 134 (2003) 1-9.
[38] J. Song, C. Song, G. Lv, L. Wang, F. Bin, Modification to Nagle/Strickland-Constable model with consideration of soot nanostructure effects, Combust. Theor. Model. 16 (2012) 639-649.
[39] J. Song, M. Alam, A. Boehman, U. Kim, Examination of the oxidation behavior of biodiesel soot, Combust. Flame 146 (2006) 589-604.
[40] K. Al-Qurashi, A.L. Boehman, Impact of exhaust gas recirculation (EGR) on the oxidative reactivity of diesel engine soot, Combust. Flame 155 (2008) 675-695.
[41] H.J. Seong, A.L. Boehman, Impact of Intake Oxygen Enrichment on Oxidative Reactivity and Properties of Diesel Soot, Energy Fuels 25 (2011) 602-616.
[42] J. Song, M. Alam, A.L. Boehman, U. Kim, Examination of the oxidation behavior of biodiesel soot, Combust. Flame 146 (2006) 589-604.
[43] R.H. Hurt, A.F. Sarofim, J.P. Longwell, Gasification-induced densification of carbons: From soot to form coke, Combust. Flame 95 (1993) 430-432.
[44] K. Kamegawa, K. Nishikubo, H. Yoshida, Oxidative degradation of carbon blacks with nitric acid (I)—

Changes in pore and crystallographic structures, Carbon 36 (1998) 433-441.